

Electronic Supplementary Material (ESI) for Nanoscale.

This journal is © The Royal Society of Chemistry 2017

Composition- and Phase-Controlled Synthesis and Applications of Alloyed Phase Heterostructures of Transition Metal Disulphides

Kai Yang^{†,a}, Xiaoshan Wang^{†,a}, Hai Li^a, Bo Chen^b, Xiao Zhang^b, Shaozhou Li^c, Ning Wang^a, Hua Zhang^b, Xiao Huang^{*,a}, Wei Huang^{*,a,c}

^a Key Laboratory of Flexible Electronics (KLOFE) & Institute of Advanced Materials (IAM), Jiangsu National Synergistic Innovation Center for Advanced Materials (SICAM), Nanjing Tech University (NanjingTech), 30 South Puzhu Road, Nanjing 211816, P.R. China

^b Center for Programmable Materials, School of Materials Science and Engineering, Nanyang Technological University, 50 Nanyang Avenue, Singapore 639798, Singapore

^c Key Laboratory for Organic Electronics and Information Displays & Institute of Advanced Materials, Jiangsu National Synergistic Innovation Center for Advanced Materials (SICAM), Nanjing University of Posts & Telecommunications, 9 Wenyuan Road, Nanjing 210023, P.R. China

[†]These authors contributed equally to this work.

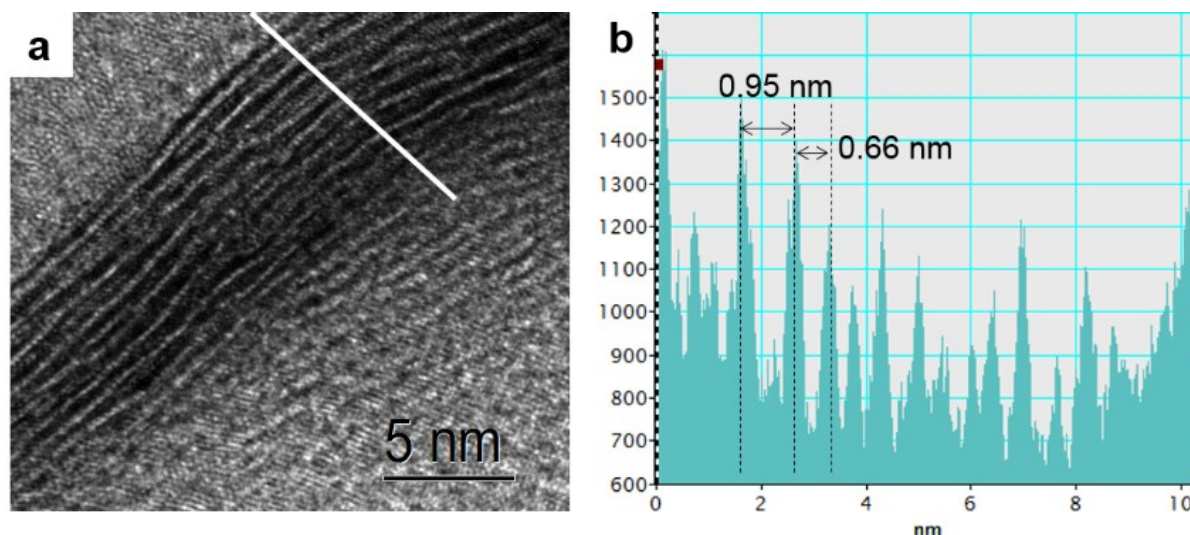


Figure S1. (a) Typical TEM image showing the edge part of Mo_{1-x}W_xS₂ nanosheet consisting of a few atomic layers. (b) Brightness profile along the white line drawn in (a) revealing that the interlayer spacing varies, typically from 0.6 to 1.0 nm.

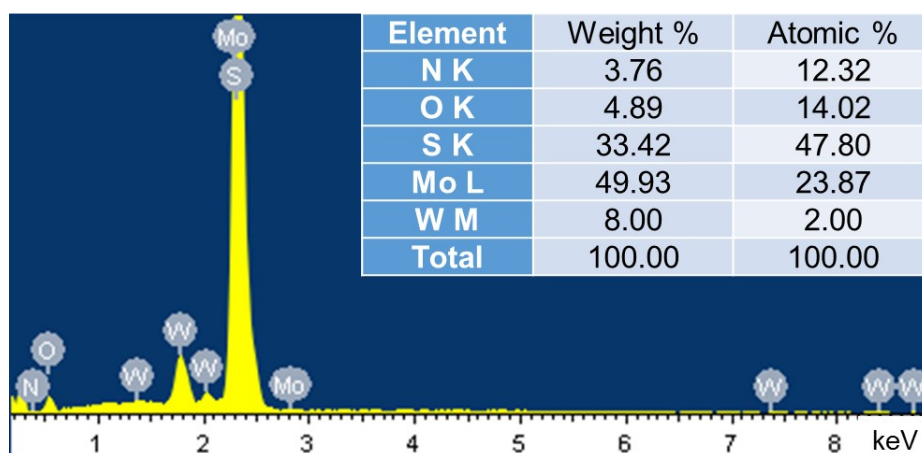


Figure S2. EDX spectrum of typical $\text{Mo}_{1-\chi}\text{W}_\chi\text{S}_2$ nanosheets synthesized at 220 °C, showing a W : Mo atomic ratio of ~1 : 11, or the χ value is ~0.08.

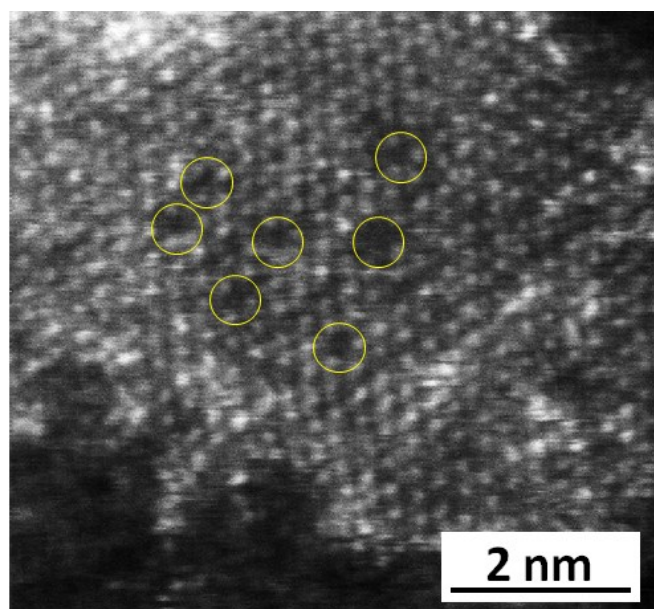


Figure S3. HR-STEM image of a typical $\text{Mo}_{1-\chi}\text{W}_\chi\text{S}_2$ nanosheet showing sulfur vacancies which are highlighted by yellow circles.

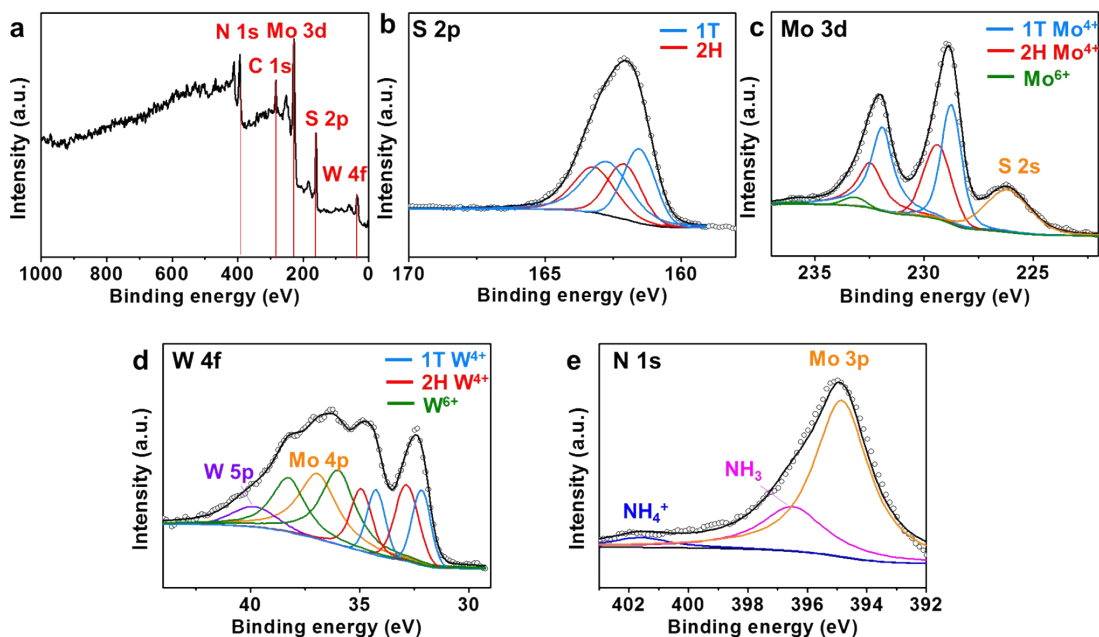


Figure S4. XPS (a) full scan, (b) S 2p, (c) Mo 3d, (d) W 4f spectra and (e) N 1s spectra of as-prepared 60 % 1T $\text{Mo}_{0.92}\text{W}_{0.08}\text{S}_2$ nanosheets synthesized at 220 °C .

As shown in **Figure S4a**, the W, Mo, S and N elements can be detected in the full scan spectrum. The high resolution S 2p spectrum in **Figure S4b** can be deconvoluted to give two sets of doublet peaks, attributable to the S^{2-} in the 1T (161.5 and 162.7 eV) and 2H (162.3 and 163.5 eV) structures, respectively.^{1,2} In the high resolution Mo 3d spectrum (**Figure S4c**), two sets of doublet peaks can be assigned to Mo^{4+} in the 1T (228.8 and 231.9 eV) and 2H (229.4 and 232.6 eV) structures, respectively.^{1,3} The peak at 226.2 eV is attributed to S 2s.^{1,3} The high resolution W 4f spectrum (**Figure S4d**) reveals three sets of doublet peaks for 1T W^{4+} (32.2 and 34.2 eV), 2H W^{4+} (32.8 and 34.9 eV), and W^{6+} (36.0 and 38.3 eV), respectively.⁴⁻⁶ It can be seen that compared to MoS_2 , WS_2 is more prone to oxidation.⁷ Besides, the W 5p (39.8 eV) and Mo 4p (36.9 eV) peaks can also be observed.^{4,5} The high resolution N 1s spectrum (**Figure S4e**) can be deconvoluted to give three peaks, assignable to NH_4^+ (401.4 eV),⁸ NH_3 (396.4 eV)⁸ and Mo 3p (394.6 eV).⁹

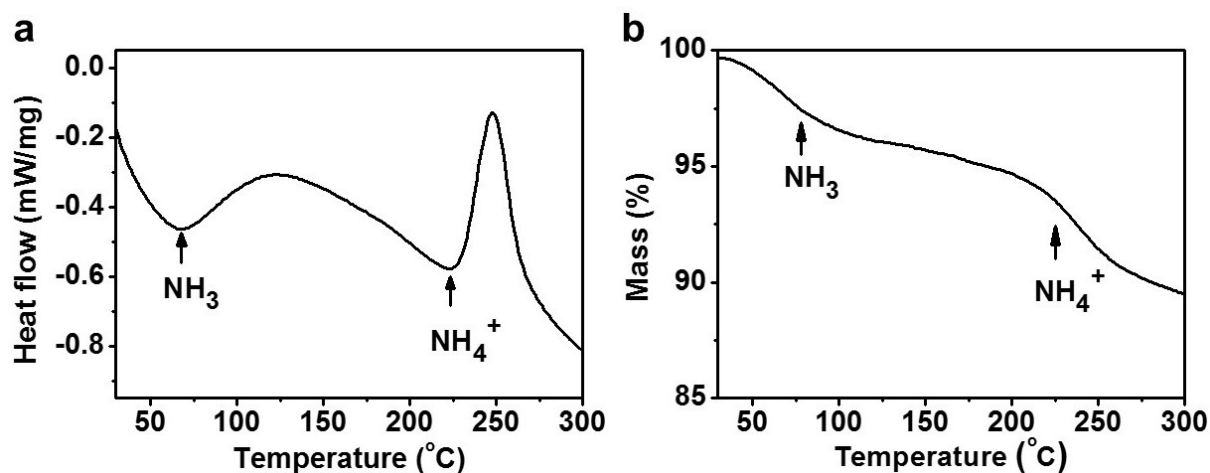


Figure S5. (a) DSC and (b) TGA results of 60% 1T $\text{Mo}_{0.92}\text{W}_{0.08}\text{S}_2$ nanosheets, showing two endothermic steps which correspond to the removal of NH_3 at around 75 °C and NH_4^+ ions at around 225 °C.

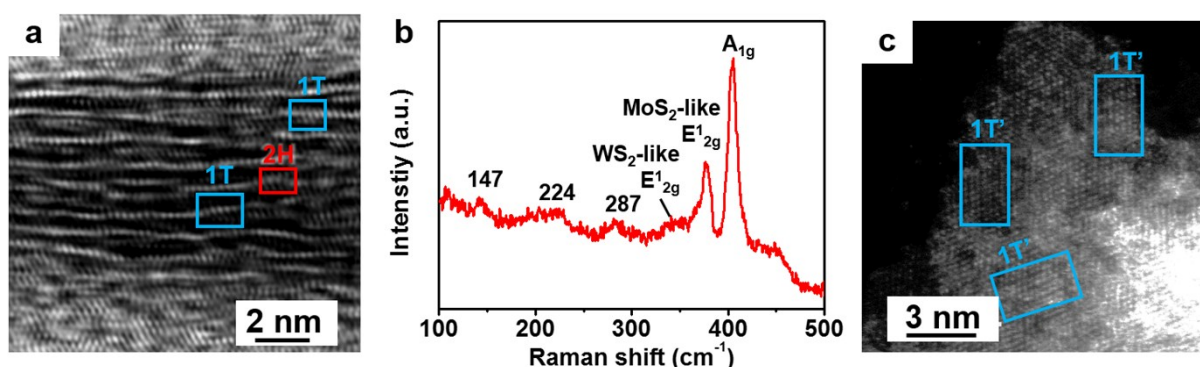


Figure S6. (a) HRTEM side-view of a typical 60% 1T $\text{Mo}_{0.92}\text{W}_{0.08}\text{S}_2$ nanosheet showing the randomly stacked layers with varied interlayer spacings. Some 1T and 2H domains are highlighted with blue and red rectangles, respectively. (b) Raman spectrum of the as-prepared $\text{Mo}_{0.92}\text{W}_{0.08}\text{S}_2$ nanosheets. (c) HR-STEM image of a typical 60% 1T $\text{Mo}_{0.92}\text{W}_{0.08}\text{S}_2$ nanosheet revealing the presence of 1T' domains.

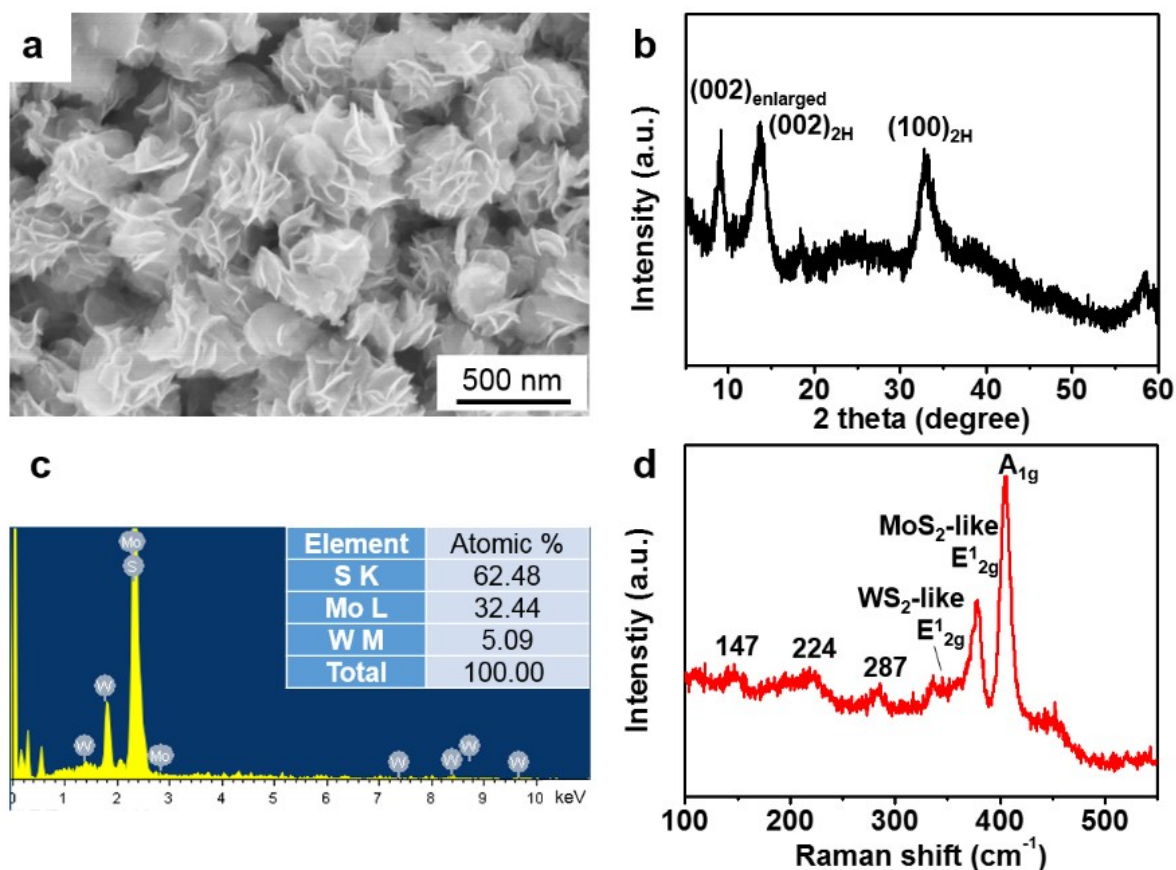


Figure S7. (a) SEM image, (b) XRD pattern, (c) EDX spectrum and (d) Raman spectrum of 30% 1T $\text{Mo}_{0.87}\text{W}_{0.13}\text{S}_2$ nanosheets prepared at 240 °C.

The 30% 1T $\text{Mo}_{0.87}\text{W}_{0.13}\text{S}_2$ nanosheets show the flower-like morphology as shown in **Figure S7a**. The XRD peaks (**Figure S7b**) positioned at 8.9°, 14° and 33° can be assigned to $(002)_{\text{enlarged}}$, $(002)_{2\text{H}}$ and $(100)_{2\text{H}}$ planes, respectively. The EDX spectrum (**Figure S7c**) indicates the W : Mo atomic ratio of $\sim 1 : 6.4$, suggesting the formation of $\text{Mo}_{0.87}\text{W}_{0.13}\text{S}_2$. Raman spectrum (**Figure S7d**) shows three peaks at 403, 377 and 346 cm^{-1} corresponding to the MoS_2/WS_2 A_{1g} , MoS_2 -like E_{2g}^1 and WS_2 -like E_{2g}^1 modes. The 1T' phase Raman active modes (147 cm^{-1} , 224 cm^{-1}) in the lower frequency region can be observed as well.¹⁰ The small peak at 287 cm^{-1} can be assigned to 2H phase.¹¹

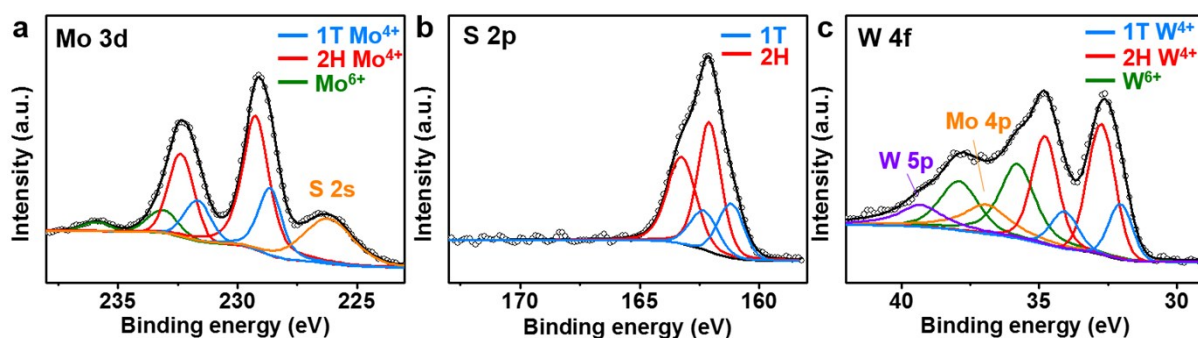


Figure S8. XPS (a) Mo 3d, (b) S 2p and (c) W 4f spectra of as-prepared 30% 1T $\text{Mo}_{0.87}\text{W}_{0.13}\text{S}_2$ nanosheets synthesized at 240 °C.

In the high resolution Mo 3d spectrum (**Figure S8a**), three sets of doublet peaks for Mo^{4+} with the 1T (228.6 and 231.7 eV) and 2H (229.2 and 232.4 eV) structures and Mo^{6+} (235.9 and 233.12 eV) can be observed.^{1,3} The peak at 226.2 eV is attributed to S 2s.^{1,3} The high resolution S 2p spectrum in **Figure S8b** can be deconvoluted to give two sets of doublet peaks, attributable to the S^{2-} in the 1T (161.2 and 162.3 eV) and 2H (162.1 and 163.3 eV) structures, respectively.^{1,2} The high resolution W 4f spectrum (**Figure S8c**) reveals three sets of doublet peaks for 1T W^{4+} (32.0 and 34.1 eV), 2H W^{4+} (32.7 and 34.8 eV) and W^{6+} (35.8 and 37.9 eV), respectively.^{4,6} In addition, the W 5p (39.3 eV) and Mo 4p (36.9 eV) peaks can also be observed.^{4,5}

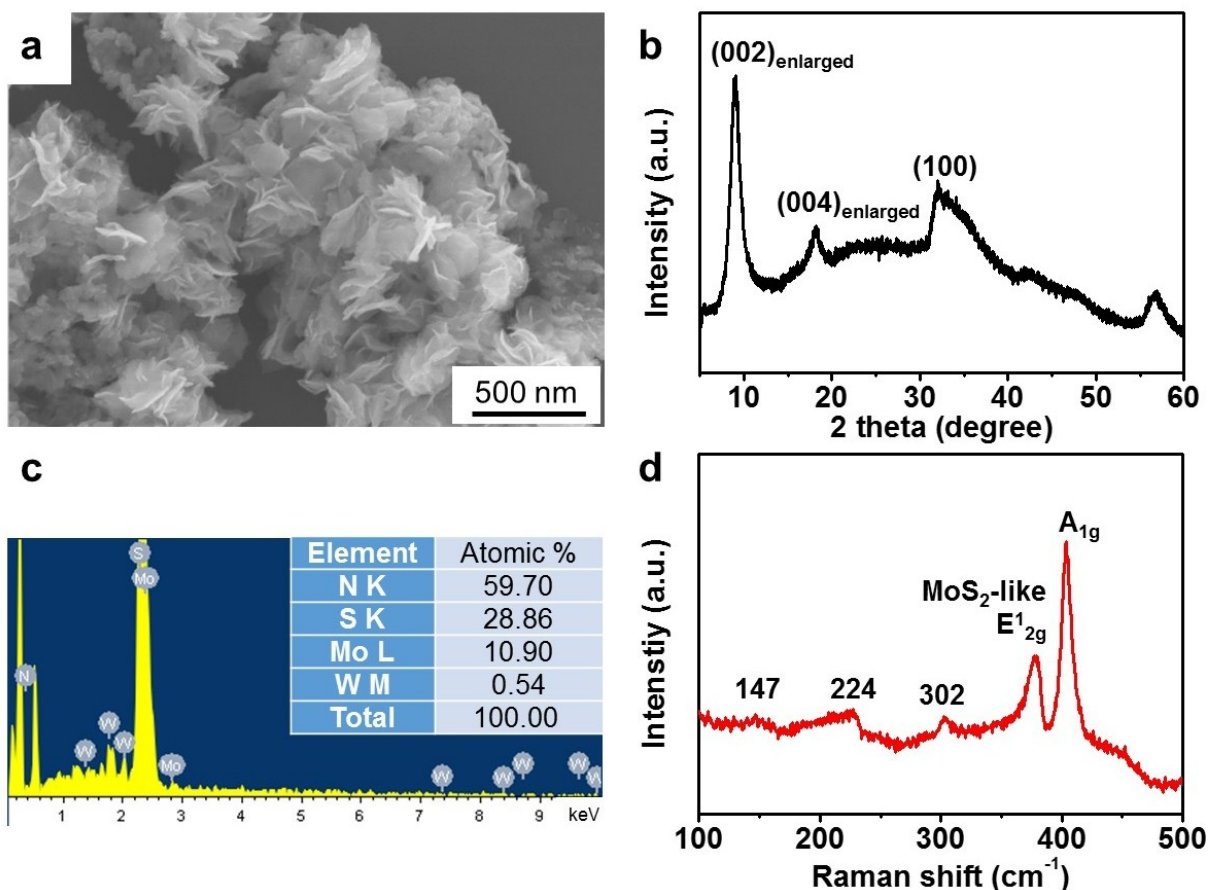


Figure S9. (a) SEM image, (b) XRD pattern, (c) EDX spectrum and (d) Raman analysis of 80% 1T $\text{Mo}_{0.96}\text{W}_{0.04}\text{S}_2$ nanosheets prepared at 200 °C.

The 80% 1T $\text{Mo}_{0.96}\text{W}_{0.04}\text{S}_2$ nanosheets show the flower-like morphology as shown in **Figure S9a**. The XRD peaks (**Figure S9b**) positioned at 8.9°, 18° and 33° can be assigned to $(002)_{\text{enlarged}}$, $(004)_{\text{enlarged}}$ and (100) planes, respectively. The EDX spectrum (**Figure S9c**) indicates the W : Mo atomic ratio of $\sim 1 : 20$, or $\text{Mo}_{0.96}\text{W}_{0.04}\text{S}_2$ was obtained. Raman spectrum (**Figure S9d**) shows two dominant peaks at 403 and 377 cm^{-1} corresponding to the A_{1g} and MoS_2 -like E'_{2g} bands and the distorted 1T phase Raman active modes (147 cm^{-1} , 224 cm^{-1}) in the lower frequency region can be observed as well.¹⁰ The small peak at 302 cm^{-1} can be assigned to the 2H phase.¹² Note that the WS_2 -like E'_{2g} is not observed, probably because the doping concentration of W is too low at $\sim 4\%$.

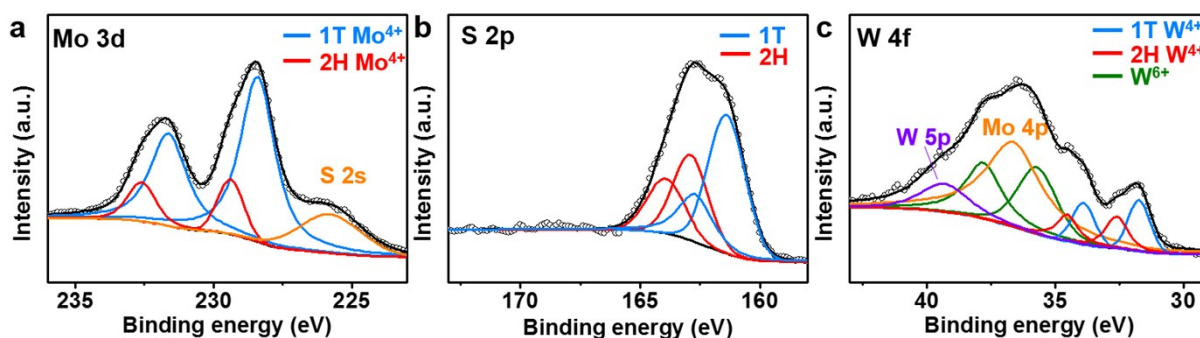


Figure S10. XPS (a) Mo 3d (b) S 2p and (c) W 4f spectra of as-prepared 80% 1T $\text{Mo}_{0.96}\text{W}_{0.04}\text{S}_2$ nanosheets prepared at 200 °C.

In the high resolution Mo 3d spectrum (**Figure S10a**), two sets of doublet peaks can be assigned to Mo^{4+} in the 1T (228.6 and 231.7 eV) and 2H (229.2 and 232.4 eV) structures.^{1,3} The peak at 226.2 eV is attributed to S 2s.^{1,3} The high resolution S 2p spectrum in **Figure S10b** can be deconvoluted to give two sets of doublet peaks, attributable to the S^{2-} in the 1T (161.2 and 162.3 eV) and 2H (162.1 and 163.3 eV) structures, respectively.^{1,2} The high resolution W 4f spectrum (**Figure S10c**) reveals three sets of doublet peaks for 1T W^{4+} (31.7 and 33.9 eV), 2H W^{4+} (32.6 and 34.5 eV) and W^{6+} (35.7 and 37.8 eV), respectively.^{4,6} In addition, the W 5p (39.3 eV) and Mo 4p (36.6 eV) peaks can also be observed.^{4,5}

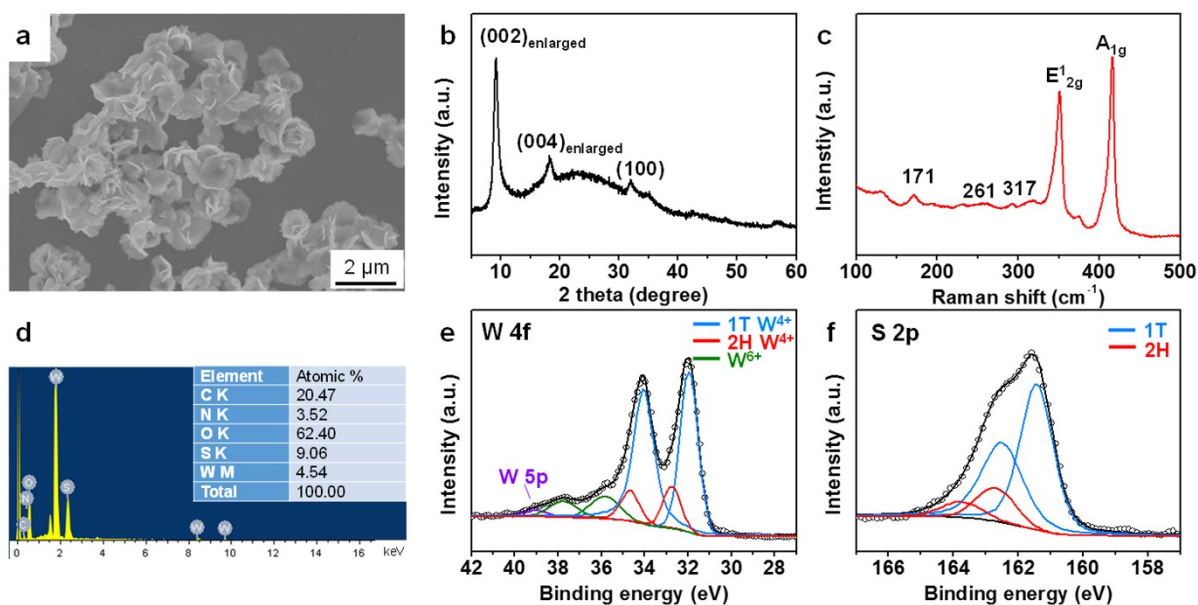


Figure S11. (a) SEM image, (b) XRD pattern, (c) Raman spectrum, (d) EDX spectrum, (e) XPS W 4f spectrum and (f) XPS S 2p spectrum of 80% 1T WS₂ nanosheets.

The 80% 1T WS₂ nanosheets show the flower-like morphology as shown in **Figure S11a**. The XRD peaks (**Figure S11b**) positioned at 8.9°, 18° and 33° can be assigned to (002)_{enlarged}, (004)_{enlarged} and (100) planes, respectively. Raman spectrum (**Figure S11c**) shows two peaks at 416 and 350 cm⁻¹ corresponding to the A_{1g}, E¹_{2g} modes. Three small WS₂ peaks (171 cm⁻¹, 261 cm⁻¹ and 317 cm⁻¹) can be observed in the lower frequency region which can be assigned to the 1T phase.¹³⁻¹⁵ The EDX spectrum (**Figure S11d**) indicates the W:S atomic ratio of ~1 : 2. The high resolution W 4f spectrum (**Figure S11e**) reveals three sets of doublet peaks for 1T W⁴⁺ (31.7 and 33.9 eV), 2H W⁴⁺ (32.6 and 34.5 eV) and W⁶⁺ (35.7 and 37.8 eV), respectively.⁴⁻⁶ The high resolution S 2p spectrum (**Figure S11f**) can be deconvoluted to give four peaks, attributable to the S²⁻ in the 1T (161.2 and 162.3 eV) and 2H (162.1 and 163.3 eV) structures, respectively.^{1,2}

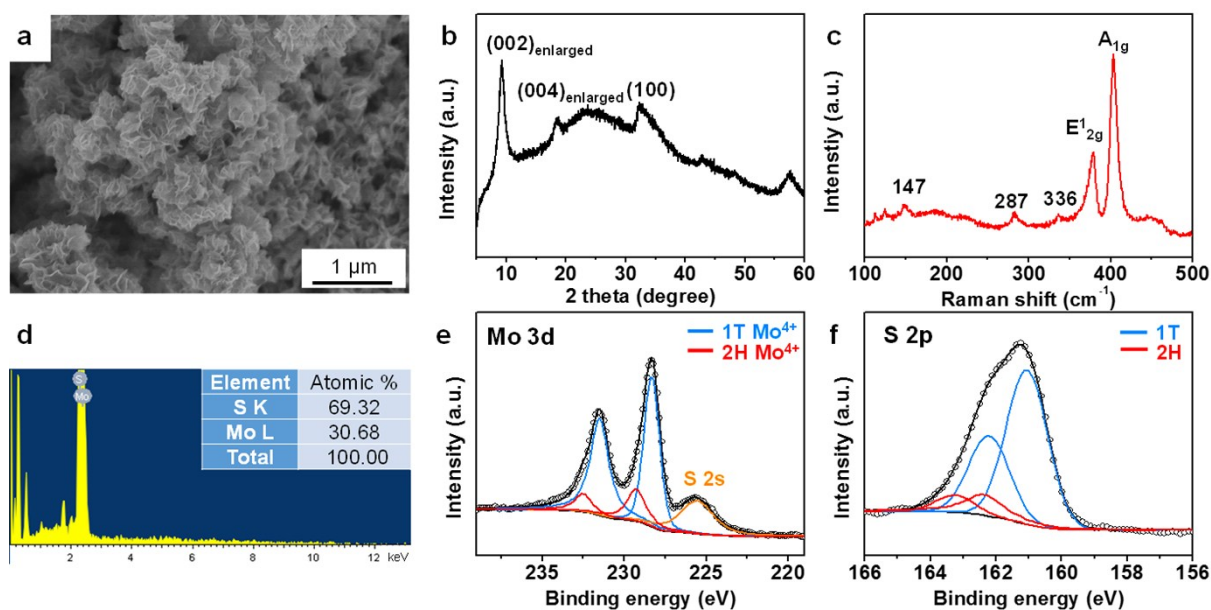


Figure S12. (a) SEM image, (b) XRD pattern, (c) Raman spectrum, (d) EDX spectrum, (e) XPS Mo 3d spectra and (f) XPS S 2p spectra of 80% 1T MoS₂ nanosheets.

The 80% 1T MoS₂ nanosheets show the flower-like morphology as shown in **Figure S12a**. The XRD peaks (**Figure S12b**) positioned at 8.9°, 18° and 33° can be assigned to (002)_{enlarged}, (004)_{enlarged} and (100) planes, respectively. Raman spectrum (**Figure S12c**) shows two peaks at 403 and 377 cm⁻¹ corresponding to the A_{1g}, E_{2g}¹ modes. The 1T' phase Raman active modes (147 cm⁻¹, 336 cm⁻¹) in the lower frequency region can be observed as well.¹⁰ The small peak at 287 cm⁻¹ can be assigned to the 2H phase.¹¹ The EDX spectrum (**Figure S12d**) indicates the Mo:S atomic ratio of ~1 : 2. The high resolution Mo 3d spectrum (**Figure S12e**) reveals two sets of double peaks, which can be assigned to Mo⁴⁺ in the 1T (228.6 and 231.7 eV) structure and 2H (229.2 and 232.4 eV) structures, respectively.^{1,3} The peak at 226.2 eV is attributed to S 2s.^{1,3} The high resolution S 2p spectrum (**Figure S12f**) can be deconvoluted to give four peaks, attributable to the S²⁻ in the 1T (161.2 and 162.3 eV) and 2H (162.1 and 163.3 eV) structures, respectively.^{1,2}

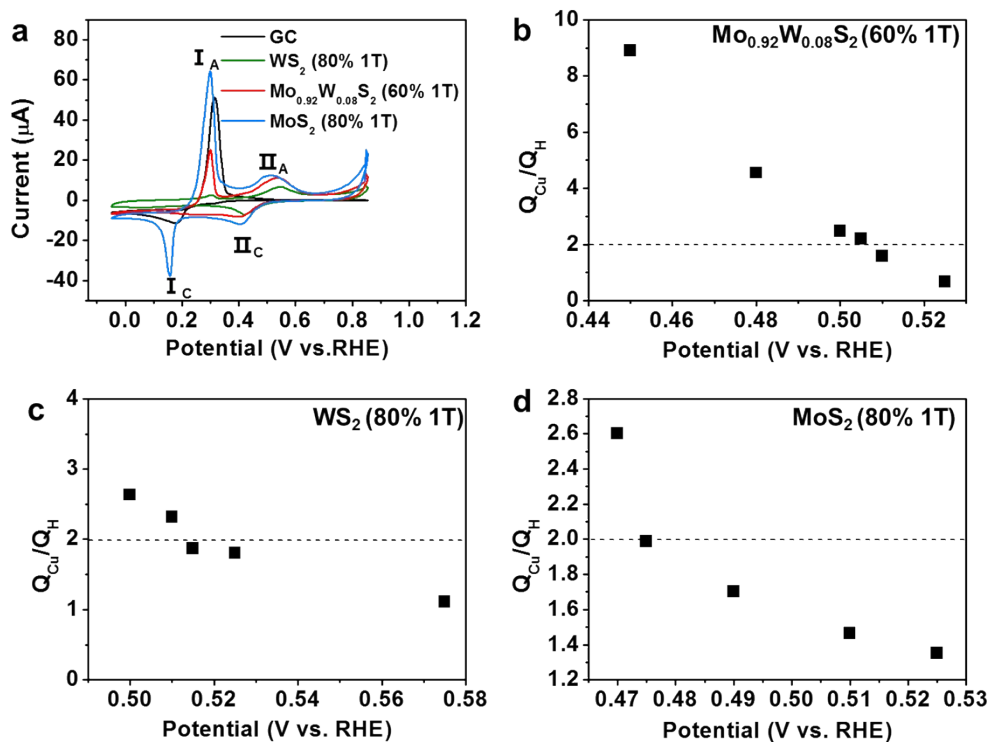


Figure S13. (a) Cyclic voltammetry (CV) measurements of different metal sulfide catalysts in presence of cupric sulfate. The sharp peaks correspond to the overpotential stripping and deposition, *i.e.* I_A and I_C , respectively. The broad peaks correspond to the underpotential regions, *i.e.* II_A and II_C , respectively. The bare glassy carbon electrode does not exhibit any underpotential deposition signal. The charge ratio for copper stripping and hydrogen adsorption, *i.e.* Q_{Cu}/Q_H , reaches 2 at 505, 510 and 475 mV vs. RHE for (b) $Mo_{0.92}W_{0.08}S_2$ (60% 1T), (c) WS_2 (80% 1T) and (d) MoS_2 (80% 1T), respectively.

To compare the catalytic activity of MoS_2 (80% 1T), WS_2 (80% 1T) and alloyed $Mo_{1-x}W_xS_2$ nanosheets, we measured their density of active sites using the copper underpotential deposition method reported previously by Green et al.¹⁶ The cyclic voltammetry (CV) measurements of different catalysts were conducted in a solution containing 0.1 M H_2SO_4 and 2 mM $CuSO_4$ with scan rate of 2 mV/s using a saturated calomel electrode as the reference electrode (**Figure S13a**). The underpotential deposition (UPD, II_A) region, which is in the higher potential compared to the thermodynamic deposition potential (overpotential deposition, OPD, I_A) region, was thus located, for example, at ~ 400 -660 mV for the 60% 1T $Mo_{0.92}W_{0.08}S_2$ based electrode. The amount of charge transferred during the UPD can be determined by conducting the following three-step process. Taking 60% 1T $Mo_{0.92}W_{0.08}S_2$ as

an example, first, in a 0.1 M of H₂SO₄ and 2 mM CuSO₄ solution, the electrode surface was electrochemically cleaned by applying a potential (*e.g.* 673 mV) higher than the UPD region for 120 s. Then, the deposition of copper was conducted at a constant potential in the range of 400-660 mV, for example 450 mV, for 100 s. After that, the voltage was gradually increased to 673 mV to oxidize the deposited copper at a scan rate of 2 mV/s, and the amount of charge transferred was recorded. Similar steps were performed for the same catalyst at the same deposition potential but in a 0.1 M of H₂SO₄ solution without the presence of CuSO₄, in order to obtain the amount of charge exchanged during the hydrogen adsorption. The charge ratio for copper stripping and hydrogen adsorption (*i.e.* Q_{Cu}/Q_H) at various deposition potentials were calculated and plotted in **Figure S13b-d**. It can be seen that the Q_{Cu}/Q_H ratio decreases with increasing the deposition potential. The Q_{Cu}/Q_H ratio of 2 is expected when the monolayer copper is deposited at the same site as that for hydrogen adsorption since copper stripping involves two electrons versus one for hydrogen adsorption. From **Figure S13b-d**, we can determine that the deposition potential to yield single-atomic layer deposition of copper is 505, 510 and 475 mV *vs.* RHE for Mo_{0.92}W_{0.08}S₂ (60% 1T), 1T WS₂ (80% 1T) and 1T MoS₂ (80% 1T), respectively. The mole number of the deposited copper (Equation 1), N_{Cu} (Equation 2) and the active site density (N_{Cu}/A_{electrode}) were calculated and listed in **Figure 4d**.

$$n_{\text{Cu}} = Q_{\text{Cu}}(C) / ((96500C/e^-)(2e^-/\text{Cu})) \quad (1)$$

$$N_{\text{Cu}} = n_{\text{Cu}}(\text{mol}) * L(\text{mol}^{-1}) \quad (2)$$

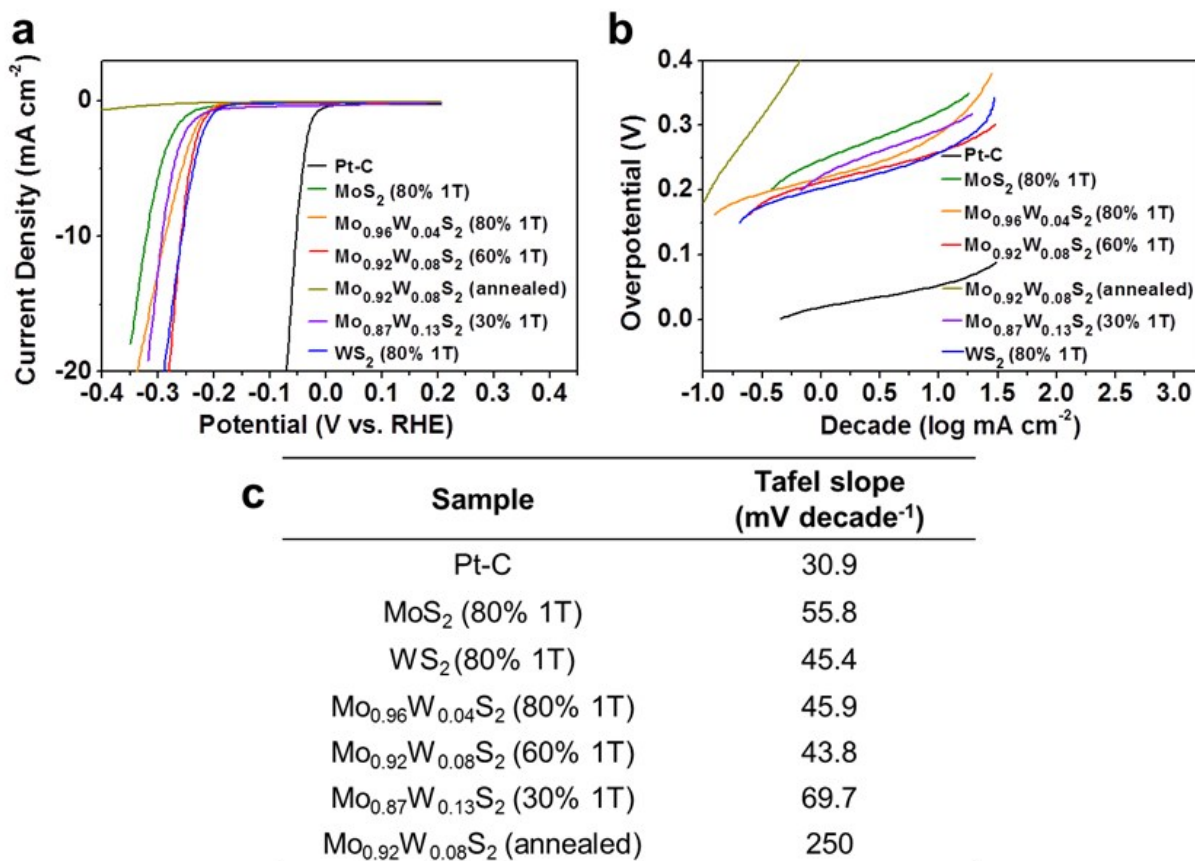


Figure S14. (a) Polarization curves of Pt-C (10 wt% of Pt), MoS_2 nanosheets (80% 1T), WS_2 nanosheets (80% 1T), $\text{Mo}_{0.96}\text{W}_{0.04}\text{S}_2$ nanosheets (80% 1T), $\text{Mo}_{0.92}\text{W}_{0.08}\text{S}_2$ nanosheets (60% 1T), $\text{Mo}_{0.92}\text{W}_{0.08}\text{S}_2$ nanosheets (annealed) and $\text{Mo}_{0.87}\text{W}_{0.13}\text{S}_2$ nanosheets (30% 1T). (b) Corresponding Tafel plots obtained from the polarization curves in (a). (c) List of Tafel slope values calculated from the Tafel plots in (b).

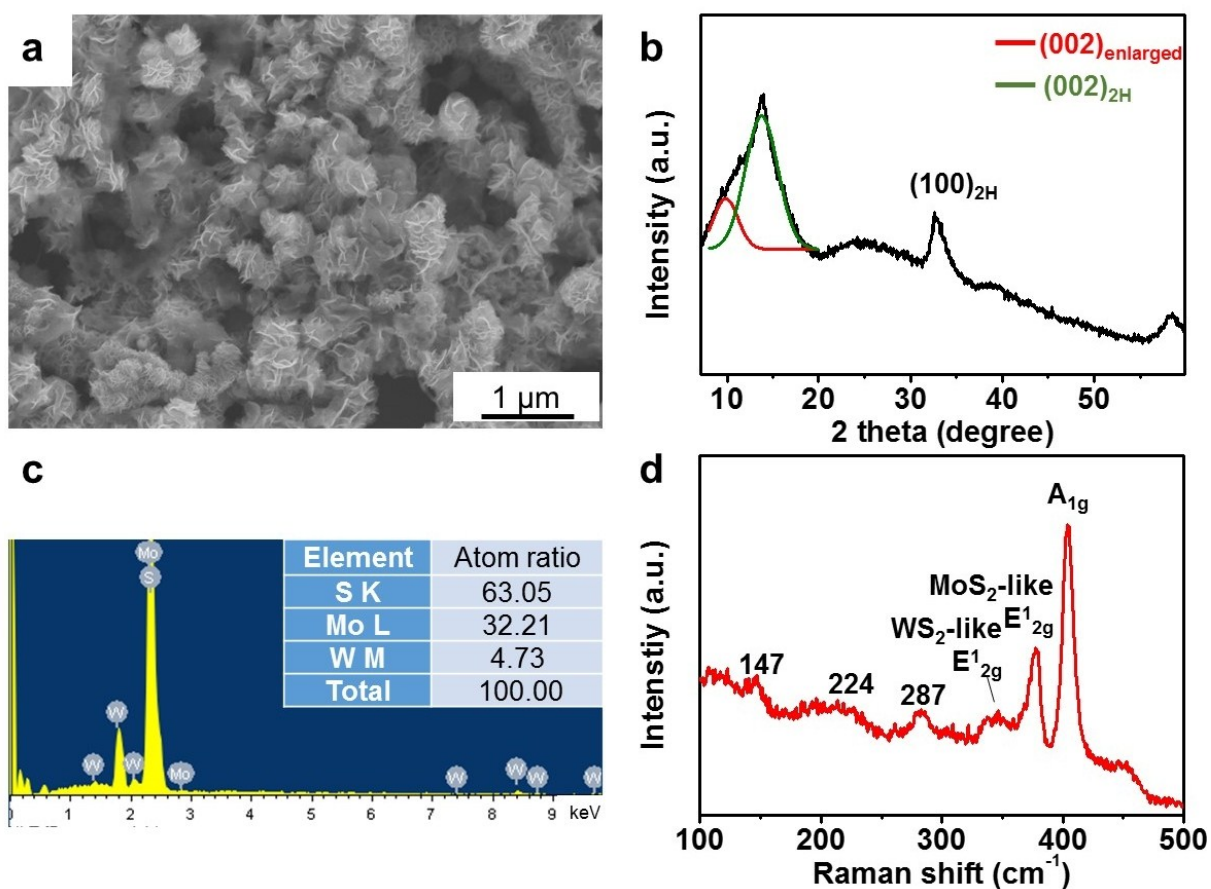


Figure S15. (a) SEM image, (b) XRD pattern, (c) EDX spectrum and (d) Raman analysis of 10% 1T $\text{Mo}_{0.87}\text{W}_{0.13}\text{S}_2$ nanosheets prepared by heating the precursor solution at 200 °C for 24 h and then at 240 °C for 24 h.

The 10% 1T $\text{Mo}_{0.87}\text{W}_{0.13}\text{S}_2$ nanosheets also show the flower-like morphology as shown in **Figure S15a**. The deconvoluted XRD peaks (**Figure S15b**) positioned at 8.9°, 14° and 33° can be assigned to $(002)_{\text{enlarged}}$, $(002)_{2\text{H}}$ and $(100)_{2\text{H}}$ planes, respectively. The EDX spectrum (**Figure S15c**) indicates a the W : Mo atomic ratio of $\sim 1 : 6.8$, or $\text{Mo}_{0.87}\text{W}_{0.13}\text{S}_2$ was obtained. Raman spectrum (**Figure S15d**) shows two dominant peaks at 403 and 377 cm^{-1} corresponding to the A_{1g} and MoS_2 -like E^1_{2g} bands. The distorted 1T' phase Raman active modes (147 cm^{-1} , 224 cm^{-1}) in the lower frequency region can be observed as well.¹⁰ The small peak at 287 cm^{-1} can be assigned to the 2H structure.¹¹

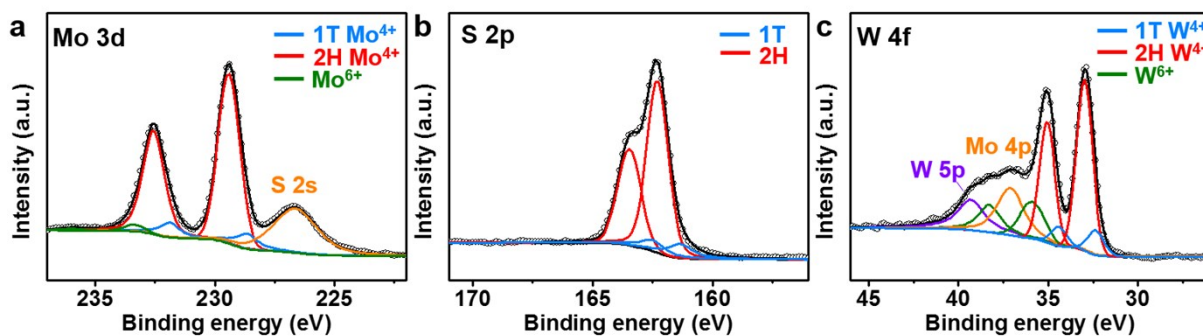


Figure S16. XPS spectra of (a) Mo 3d (b) S 2p and (c) W 4f of as-prepared 10% 1T $\text{Mo}_{0.87}\text{W}_{0.13}\text{S}_2$ nanosheets.

In the high resolution Mo 3d spectrum (**Figure S16a**), three sets of doublet peaks for Mo^{4+} in the 1T (228.6 and 231.7 eV) and 2H (229.2 and 232.4 eV) structures and Mo^{6+} (235.9 and 233.12 eV) can be found observed.^{1,3} The peak at 226.2 eV is attributed to S 2s.^{1,3} The high resolution S 2p spectrum in **Figure S16b** can be deconvoluted to give two sets of doublet peaks, attributable to the S^{2-} in the 1T (161.2 and 162.3 eV) and 2H (162.1 and 163.3 eV) structures, respectively.^{1,2} The high resolution W 4f spectrum (**Figure S16c**) reveals three sets of doublet peaks for 1T W^{4+} (31.7 and 33.9 eV), 2H W^{4+} (32.6 and 34.5 eV) and W^{6+} (35.7 and 37.8 eV), respectively.⁴⁻⁶ Besides In addition, the W 5p (39.3 eV) and Mo 4p (36.6 eV) peaks can also be observed.^{4,5}

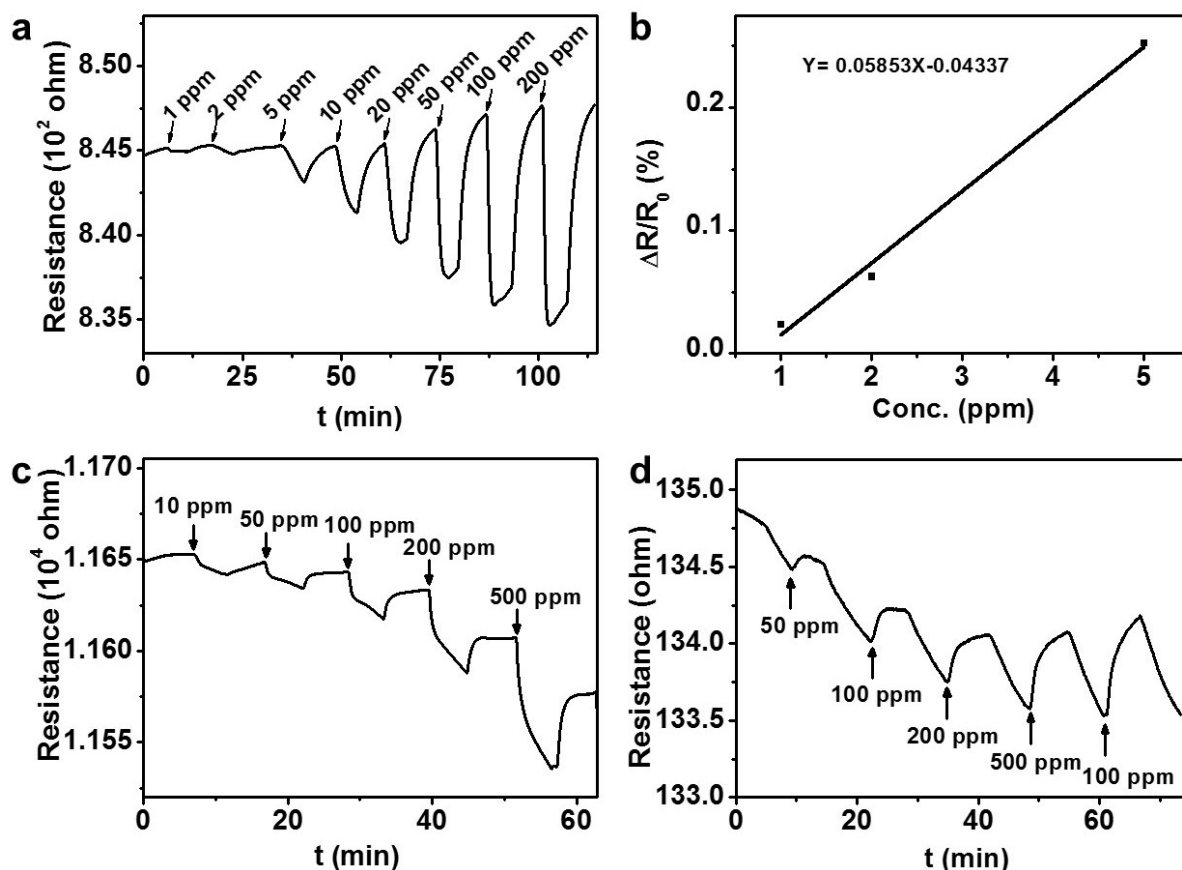


Figure S17. (a) Dynamic sensing performance of a sensor based on $\text{Mo}_{0.87}\text{W}_{0.13}\text{S}_2$ (10% 1T) nanosheets towards acetone gas at different concentrations. (b) Linear fit of the response versus acetone concentration for of 1-5 ppm acetone. The limit of detection (LOD) was calculated at a sensitivity of 3 times of signal to noise ratio, *i.e.* 0.002%, to be 0.7 ppm. Dynamic sensing performance of a sensor based on (c) annealed $\text{Mo}_{0.87}\text{W}_{0.13}\text{S}_2$ and (d) $\text{Mo}_{0.87}\text{W}_{0.13}\text{S}_2$ (30% 1T) towards acetone gas at different concentrations.

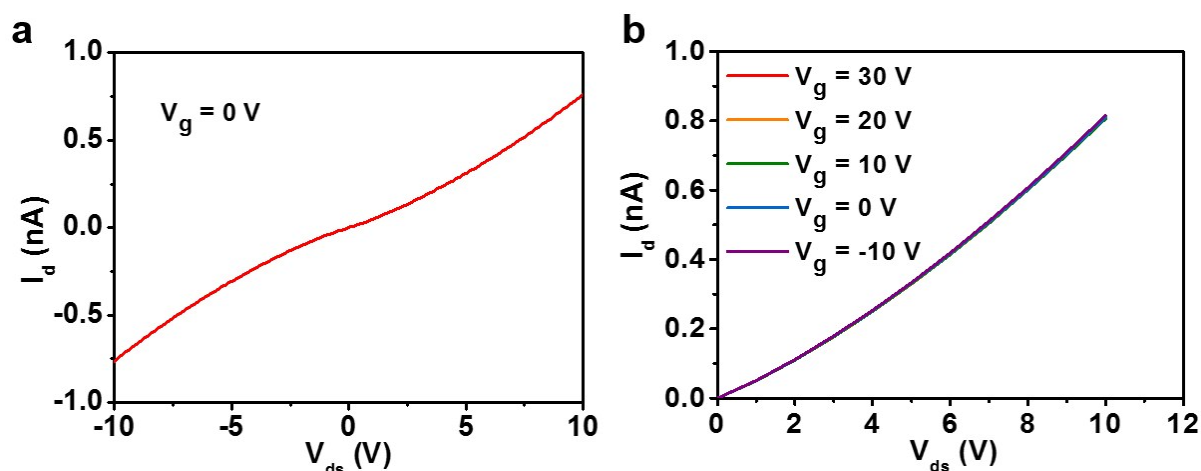


Figure S18. (a) I_d - V_{ds} characteristics of a back-gated thin film FET based on as-prepared $\text{Mo}_{0.87}\text{W}_{0.13}\text{S}_2$ (30% 1T) nanosheets at $V_g = 0$ V, and (b) the I_d - V_{ds} curves of the FET at various V_g measured in vacuum (5×10^{-5} Torr) at 100 K.

Reference

1. Q. Ding, F. Meng, C. R. English, M. Cabán-Acevedo, M. J. Shearer, D. Liang, A. S. Daniel, R. J. Hamers and S. Jin, *J. Am. Chem. Soc.*, 2014, **136**, 8504-8507.
2. H. Liu, K. K. Antwi, S. Chua and D. Chi, *Nanoscale*, 2014, **6**, 624-629.
3. G. Eda, H. Yamaguchi, D. Voiry, T. Fujita, M. W. Chen and M. Chhowalla, *Nano Lett.*, 2011, **11**, 5111-5116.
4. J. Yang, D. Voiry, S. J. Ahn, D. Kang, A. Y. Kim, M. Chhowalla and H. S. Shin, *Angew. Chem. Int. Ed.*, 2013, **52**, 13751-13754.
5. F. M. Wang, J. S. Li, F. Wang, T. A. Shifa, Z. Z. Cheng, Z. X. Wang, K. Xu, X. Y. Zhan, Q. S. Wang, Y. Huang, C. Jiang and J. He, *Adv. Funct. Mater.*, 2015, **25**, 6077-6083.
6. B. Mahler, V. Hoepfner, K. Liao and G. A. Ozin, *J. Am. Chem. Soc.*, 2014, **136**, 14121-14127.
7. M. A. Lukowski, A. S. Daniel, C. R. English, F. Meng, A. Forticaux, R. J. Hamers and S. Jin, *Energ. Environ. Sci.*, 2014, **7**, 2608-2613.
8. Q. Liu, X. Li, Q. He, A. Khalil, D. Liu, T. Xiang, X. Wu and L. Song, *Small*, 2015, **11**, 5556-5564.
9. G. T. Kim, T. K. Park, H. S. Chung, Y. T. Kim, M. H. Kwon and J. G. Choi, *Appl. Surf. Sci.*, 1999, **152**, 35-43.
10. P. Cheng, K. Sun and Y. H. Hu, *Nano Lett.*, 2016, **16**, 572-576.
11. Y. F. Chen, D. O. Dumcenco, Y. M. Zhu, X. Zhang, N. N. Mao, Q. L. Feng, M. Zhang, J. Zhang, P. H. Tan, Y. S. Huang and L. M. Xie, *Nanoscale*, 2014, **6**, 2833-2839.
12. D. O. Dumcenco, K. Y. Chen, Y. P. Wang, Y. S. Huang and K. K. Tiong, *J. Alloy. Compd.*, 2010, **506**, 940-943.
13. Q. J. Xiang, J. G. Yu and M. Jaroniec, *J. Am. Chem. Soc.*, 2012, **134**, 6575-6578.
14. Q. Liu, X. Li, Z. Xiao, Y. Zhou, H. Chen, A. Khalil, T. Xiang, J. Xu, W. Chu, X. Wu, J. Yang, C. Wang, Y. Xiong, C. Jin, P. M. Ajayan and L. Song, *Adv. Mater.*, 2015, **27**, 4837-4844.
15. D. Voiry, H. Yamaguchi, J. Li, R. Silva, D. C. Alves, T. Fujita, M. Chen, T. Asefa, V. B. Shenoy, G. Eda and M. Chhowalla, *Nat. Mater.*, 2013, **12**, 850-855.
16. C. L. Green and A. Kucernak, *J. Phys. Chem. B*, 2002, **106**, 1036-1047.